Journal of Electron Spectroscopy and Related Phenomena 266 (2023) 147368

Contents lists available at ScienceDirect

Journal of Electron Spectroscopy and Related Phenomena

journal homepage: www.elsevier.com/locate/elspec

Scanning transmission soft X-ray spectromicroscopy of mouse kidney and liver

Tuomas Mansikkala [a,b], Takuji Ohigashi [c], Miia H. Salo [b,d], Anniina E. Hiltunen [d], Reetta Vuolteenaho [b], Petra Sipilä [e], Satu Kuure [f,g], Marko Huttula [a], Johanna Uusimaa [d,h], Reetta Hinttala [b,d], Ilkka Miinalainen [b], Salla Kangas [d], Minna Patanen [a,b,*]

[a] Nano and Molecular Systems Research Unit, University of Oulu, PO Box 3000, 90014 Oulu, Finland
[b] Biocenter Oulu, PO Box 5000, 90014 Oulu, Finland
[c] UVSOR Synchrotron Facility, Institute for Molecular Science, Okazaki 444-8585, Japan
[d] Research Unit of Clinical Medicine and Medical Research Center, Oulu University Hospital and University of Oulu, 90014 Oulu, Finland
[e] Research Centre for Integrative Physiology and Pharmacology, and Turku Center for Disease Modeling, Institute of Biomedicine, University of Turku, 20014 Turku, Finland
[f] Stem Cells and Metabolism Research, Program, Faculty of Medicine, University of Helsinki, 00014 Helsinki, Finland
[g] GM-Unit, Laboratory Animal Center, Helsinki Institute of Life Science, University of Helsinki, 00014 Helsinki, Finland
[h] Clinic for Children and Adolescents, Oulu University Hospital, 90029 Oulu, Finland

ARTICLE INFO

Keywords:
Scanning transmission X-ray microscopy
X-ray absorption spectroscopy
Spectromicroscopy
Biological specimen
Lysosomal storage disease
Slc17a5

ABSTRACT

Scanning transmission X-ray microscopy (STXM) in the soft X-ray range is well-suited to study ultrastructural features of mammalian soft tissues. Especially at the carbon 1s edge, the imaging contrast varies drastically across the edge due to rapid changes in the X-ray absorption cross-section of functional groups present in the tissue samples enabling label-free soft X-ray spectromicroscopic studies. We present STXM spectromicroscopic imaging of mouse kidney and liver tissues. We especially concentrate on ultrastructural abnormalities in genetically modified *Slc17a5* mice. STXM is a promising technique to study storage diseases without chemical alteration due to staining agents, but sample preparation poses a challenge.

1. Introduction

An X-ray image of Anna Bertha Ludwig's hand is one of the most famous X-ray images ever taken. Wilhelm Conrad Röntgen took the image 1895, and it shows a clear contrast between his wife's bones and a wedding ring with a grey shadow from the soft tissue. Röntgen conducted a series of experiments to characterize the new rays he had discovered and reported for example that "*molecules obstruct the X-rays, the more effectively as the density of the body concerned is greater*" and "*the geometrical arrangement of the molecules might affect the action of a body upon the X-rays*" [1]. Very early on these properties of X-rays were harnessed to be used in medical diagnostics as well as materials research, and today, the X-ray imaging is a standard characterization technique in various fields yet still under constant development.

In order to focus X-rays, special optics needed to be developed due to less than 1 refractive index. Kirkpatrick and Baez used grazing-incidence geometry to construct the first X-ray microscope [2]. Synchrotron radiation facilities with superior brilliance compared to X-ray tubes and a possibility to tune the photon energy started the era of soft X-ray spectromicroscopy. The first scanning X-ray microscope using synchrotron radiation was in operation in 1972 at Cambridge Electron Accelerator [3]. In their first setup, the X-ray beam was cut to approximately 2 μm using a pinhole, and no monochromator was used. The sample was raster scanned perpendicular to the X-ray beam, and fluorescent signal was collected behind the sample using gas-filled proportional counters. Owing to element specific fluorescent emission, they were able to record elemental maps of samples. In the following years, the continuing development in many frontiers from insertion devices and monochromators to high precision sample scanners and zone plates as focusing optical elements enabled a steady advancement of the field at many synchrotron radiation facilities [4–8].

In the beginning of 1990s, spatial and spectral resolutions were demonstrated to be high enough for chemical mapping at a biologically important C 1s edge [9]. In early studies, chemical contrast especially

* Corresponding author at: Nano and Molecular Systems Research Unit, University of Oulu, PO Box 3000, 90014 Oulu, Finland.
E-mail address: minna.patanen@oulu.fi (M. Patanen).

https://doi.org/10.1016/j.elspec.2023.147368
Received 31 March 2023; Received in revised form 29 June 2023; Accepted 29 June 2023
Available online 5 July 2023

between proteins and DNA were used to study distribution of them in cells as well as packing of DNA [10,11]. Nowadays, a quantitative analysis of DNA, RNA, histone, and other proteins in chromosomes is possible, as shown in recent studies by Shinohara et al. [12,13]. Lawrence et al. carried out a multi technique study of microbial biofilms combining STXM, confocal laser scanning microscopy (CLSM), and transmission electron microscopy (TEM) imaging [14]. Near Edge X-ray Absorption Fine Structure (NEXAFS) spectra of carbonates, proteins, saccharides, lipids, and DNA have distinct features over the C 1s edge, and they used spectra of model compounds to fit STXM images recorded over an extended energy range. They presented spatial distribution of macromolecular components using color-coded composition maps, where red (R), blue (B) and green (G) colors are assigned to different macromolecular spectrum. RGB maps are visually appealing way to bring colors to the otherwise grayscale imaging and shows the power of X-ray spectromicroscopic imaging much like color photography vs. black and white photography. Lawrence et al. also performed a correlative analysis with CLSM with fluorescent stained biofilms showing that hydrated biofilms contain extracellular nucleic acids [14]. Their comparison between STXM and TEM of resin-embedded individual biofilm components demonstrated that while a typical TEM sample preparation procedure they used conserved the ultrastructure of the studied bacterium, the NEXAFS spectral features were the same when recorded from the bacterium or averaged over the whole imaged region including the polymeric matrix. This highlighted the need for advanced sample preparation methods conserving both the ultrastructural features as well as the biomolecular content of cells.

An evident way to avoid changes due to sample preparation is to use wet samples, e.g., cells grown directly on Si_3N_4 membranes in cell culture medium. Sedlmair et al. compared differently prepared vascular smooth muscle cells from an unfixed and living sample in a wet cell to a dried and fixed sample [15]. The fixation improved the absorption contrast of the cytoskeleton compared to unfixed cells, but on the other hand, analysis at the Ca 2p edge revealed that the Ca-content in dried fixed cells was only half of the Ca in dried unfixed cells. Cryo-sectioning is another way to avoid fixation and thus keep the sample preparation low. Hunter et al. studied freeze-dried, cryo-sectioned *P. aeruginosa* biofilms both at C 1s and Fe 2p edges [16]. The C 1s edge soft X-ray spectromicroscopy was used to look at the macromolecular distributions, which were dominated by a strong protein signal, and needed to be subtracted from the sample to reveal the distribution of polysaccharide and lipid components. It was concluded that sample preparation may still have altered the localization of these delicate components, and cryo preparation thus only partially overcame the problems occurring when embedding biological samples in resin.

In our earlier work, we performed soft X-ray spectromicroscopic study for cryo-sectioned, non-embedded Norway spruce cells [17]. While spectra obtained from cryo-sections were 'cleaner' compared to resin-embedded samples, the sectioning scraped off softer material inside the cells keeping the harder cell walls better intact. During the measurements, the cryo-sectioned samples were more prone to radiation damage and changed their shape. It is, however, clear that chemical information is typically better preserved in wet or cryo samples. Cryo-immobilisation is especially used in soft X-ray tomography of whole cells, where the fixed photon energy is selected to be in the "water window", i.e. between C and O 1s absorption edges to obtain 3D images of cells and subcellular structures down to a couple of tens of nm spatial resolution [18,19]. Chemical imaging in 3D, STXM spectrotomography, is also possible, but requires special attention to the sample environment, especially if spectroscopic information would be desired at C or O 1s edges due to strong absorption by glass capillaries normally used in soft X-ray tomography [20]. Spectrotomography in cryo conditions was shown to reduce the radiation damage, which is usually a problem due to extended measurement times compared to 2D spectromicroscopy or single energy tomography [21].

While wet cells and cryo-sectioning have both their benefits, these preparation methods have challenges when it comes to biological tissue samples dissected from a patient or a laboratory animal, and resin-embedding provides more resistance to radiation damage and keeps the morphology better intact. Bedolla et al. have studied paraffin-embedded rat kidney and liver tissues and compared radiation damage effects in samples with different support and fixation protocols [22]. They used single-energy soft X-ray microscopy to image the tissues and followed the chemical modification due to radiation damage with Fourier transform infrared spectroscopy. It was concluded that while the ultrastructure of tissues was preserved despite the high radiation dose in all samples, formalin fixation seemed to be the most resistant radiation damage in comparison to glutaraldehyde and Karnovsky fixations. Yamamoto et al. has performed a series of STXM studies on epoxy resin embedded samples to investigate penetration of dexamethasone, a glucocorticoid drug, into human skin [23–25]. Dexamethasone molecule has two C═O functional groups, and their O 1s → π * resonance features were found to be at slightly lower energies than in the reference skin O 1s edge X-ray absorption spectrum. This chemical shift was benefitted in the imaging by choosing the imaging energy to be on the lowest O 1s → π * resonance of dexamethasone, revealing the depth profile of the drug concentration along the tissue. In a recent study by Germer et al., the full spectral information in each pixel of STXM images was exploited to form depth profiles of rapamycin drug penetration to skin [26]. It was concluded that singular value decomposition (SVD) approach based on fitting of reference spectra in extended energy range was more sensitive way to extract the drug penetration profiles compared to approach in which differences in absorption at two selected energies is utilized.

Brooks et al. carried out a soft X-ray spectromicroscopy study at C 1s edge for resin-embedded human brain tissue samples from Parkinson's disease patients [27]. They were able to locate neuromelanin in their samples based on specific C 1s → σ * absorption feature due to C-S bonding. This demonstrates the potential of STXM as a label-free technique, as detection of neuromelanin has previously been relying on visible pigmentation since neuromelanin-specific markers have not been available. In another brain tissue study, Brooks et al. concentrated on speciation of iron in neuromelanin, utilizing spectromicroscopy at Fe 2p and O 1s edges [28]. Iron was shown to be present in ferric (Fe^{3+}) and ferrous (Fe^{2+}) forms in neuromelanin granules. In connection to their previous study related to amyloid plaque structures extracted from Alzheimer's disease patients, they have shown that resin-embedding sample preparation or X-ray irradiation at used doses do not have an impact on iron oxidation state of reference samples [29,30]. Thus, soft X-ray spectromicroscopy is a valuable tool when investigating chemical changes due to oxidative stress in human tissues.

The natural contrast provided by rapidly varying cross-section at core level absorption edges motivated us to investigate whether STXM could be a suitable technique for studying storage diseases. Our interest has been especially on lysosomal storage diseases (LSDs) of Finnish disease heritage [31]. LSDs are typically rare disorders where certain material starts to accumulate to cells due to a defect in a gene affecting the function of certain enzymes responsible for transport or catabolism of macromolecules. Diagnostic tools for different LSDs vary, but TEM is commonly used to observe ultrastructural changes caused by accumulating substances [32]. Despite being rare disorders, LSDs share similar pathophysiological mechanisms, and their characterization and understanding can contribute to development of diagnostics and novel treatments across the broad spectrum of LSDs with varying clinical phenotypes [33]. The LSD chosen for this study is Salla disease (SD, OMIM # 604369) manifested by the accumulation of sialic acid (SA) in lysosomes [34,35]. SD is autosomal recessive disorder characterized by neurodegenerative symptoms and white matter abnormalities seen as hypomyelination and progressive global cerebral volume loss. SD belongs to Finnish disease heritage [36] and is manifesting with hypotonia during the first year of life, followed by variations of progressive neurological problems, including seizures and movement disorders,

however, patients usually survive into adulthood [34,35]. SD is caused by a variant in the SLC17A5 gene that encodes sialin, a lysosomal membrane protein that transports the charged sugar, N-acetylneuraminic acid, or sialic acid out of lysosomes. Impaired function of sialin causes the SA accumulation [35]. Patients with SD store approximately 10–100 times the normal amounts of free SA in their tissues and excrete 10–100 times normal amounts in the urine. Electron microscopy of patient skin biopsies and patient derived fibroblasts showed cytoplasm filled with clear vacuoles, minority of which contained amorphous weakly OsO_4-stained material [34].

One way to study diseases is to use genetically modified mouse models. The sialin in mouse has been shown to be very homologous to humans and *Slc17a5* knockout mice reproduce the basic pathogenic events of human *SLC17A5* disorders [37]. It has been shown that knockout mice which lack sialin have lysosomal SA accumulations, confirmed with lysosomal marker LAMP-1. SA accumulation was reported in both central and peripheral nervous system, but also in other tissues like liver, stomach and pancreas [37].

In the course of our investigation of LSDs, we have generated a new genetically modified *Slc17a5* mouse model and performed STXM analyses on its kidney and liver tissues. We were interested in finding out if this modification leads to similar manifestations of disease in mice as has been reported in humans. We compared the ultrastructural changes in the disease model mice tissues to healthy control mice and recorded X-ray absorption spectra over C and O 1s edges of these tissues providing spectra for various cell parts.

2. Experimental

Tissue samples were collected from 2-day-old wild type healthy control and gene modified *Slc17a5* mice after euthanasia. Gene modified mice were compound heterozygotes for insertion-deletion mutations that lead to frameshift and premature stop codon in exon 2 of *Slc17a5* gene. The gene modified mouse line was generated by Biocenter Oulu Transgenic and Tissue phenotyping core facility as part of the FinnDis-Mice project (https://www.fingmice.fi/finndismice/). The study protocol has been approved by Regional State Administrative Agency for Southern Finland (ESAVI/33743/2019).

The tissue samples were fixed in 4% paraformaldehyde and 2.5% glutaraldehyde in 0.1 M phosphate-buffered saline. Prior to embedding in resin some samples were stained with 1% OsO_4 and/or uranyl acetate for complementary TEM imaging at Biocenter Oulu using a Tecnai G2 Spirit 120 kV TEM (FEI, Eindhoven, The Netherlands) equipped with a Quemesa CCD camera (Olympus Soft Imaging Solutions GmbH, Münster, Germany). For STXM imaging most of the samples were left unstained to prevent possible chemical alterations from the staining agents. Few of the stained TEM samples were imaged to see if the staining agents had large impact on the spectra. The samples were embedded in either EPON resin (glycerol polyglycidyl ether, LX 112, Ladd Research) (for TEM imaging), or in 1:1 ratio of trimethylolpropane triglycidyl ether (TTE) and 4,4′-methylenebis(2-methylcyclohexylamine) (MMHA), TTE:MMHA (for STXM imaging). They were then cut to thin slices of either 70 nm (TEM imaging) or 150–200 nm (STXM imaging) thick, with x- and y-dimensions being ~250–400 μm and ~300 μm, respectively. The slices were then mounted on circular copper grids (diameter ~3 mm) with Butvar B-98 (polyvinyl butyral resin) film. Optical microscopy images of thin sections are presented in the Supplementary Material.

STXM experiments were carried out at BL4U beamline at UVSOR-III, Okazaki, Japan [38,39] and Soft*i*MAX beamline at MAX IV Laboratory, Lund, Sweden [40]. The step size in scans varies through the energy range. For C 1s edge, the used energy steps were 0.5 eV for 280–284 eV, 0.1 eV for 284–290 eV, 0.2 eV for 290–295 eV and 1 eV step for 295–300 eV. For O 1s edge the energy steps were 1 eV for 525–530 eV, 0.1 eV for 530–537 eV and 0.5 eV for 537–550 eV. The dwell times were 2 ms for both O and C 1s edges with the exception of wild type mouse kidney sample (Fig. 4) having dwell time of 4 ms. The energy calibration was done with CO_2 gas, with C 1s → 3 s transition at 292.74 eV [41] and O 1s → π * transition at 535.4 eV [42]. The spectra from each different experiment were aligned, by determining the energy differences of known peaks in each experiment and shifting the energies accordingly. The spatial resolution was limited by the selected step size which varied between approximately 190 and 330 nm.

Both C 1s and O 1s measurements were taken from similar areas within each sample, but exactly same spots were avoided to minimize the effects of radiation damage from a previous scan. In disease samples measurements were taken from areas where ultrastructural changes were detected and in control samples similar parts of the tissue were chosen. Consecutive sections from the same tissue samples were used in TEM and STXM imaging as well as during different STXM experimental campaigns. Each thin section removes 70–200 nm of the sample material, so even the same cell can appear a bit different in different sections.

Data analysis has been carried out using aXis2000 software [43]. Eventual drifting of images were corrected using alignment procedures implemented to the aXis2000 package [44]. The images are converted to optical densities (OD) using a reference spectrum I_0 measured from an empty area outside the tissue section, consisting only of the Butvar-film of the TEM-grids. The spectra shown in the following figures are presented as observed with the exception of setting the baseline of each spectrum to 0 and focusing the energy range on major features instead of the whole range. No normalization nor resin subtraction was done to the presented STXM images or spectra.

3. Results and discussion

3.1. Kidney

Kidney is a vital organ filtrating blood. The functional units of kidney, nephrons, consist of renal corpuscle with tuft of capillaries (glomerulus) and a glomerular capsule, and a nephron tubuli, which are responsible for reabsorption and secretion as well as primary urine transit to the collecting duct system. Fig. 1a) shows a TEM image of a healthy control (wild type) mouse kidney and Fig. 1b) shows the kidney of a genetically modified *Slc17a5* mouse. The samples have been stained with OsO_4 and uranyl acetate for a better contrast. With this method especially the dark concave disc-shaped cross-sections of red blood cells are easily identifiable in control kidneys, but vessels where a blood cell fills the whole capillary are also detected. Tubuli consist of several cells whose nuclei are clearly visible due to their regular shape defined by dark membrane and electron-dense heterochromatin (densely packed chromosomes) inside them. The genetically modified *Slc17a5* mouse kidney has numerous vacuoles in the tubuli. This vacuolization is in line what has generally been observed in other tissues of SD patients [34] and *Slc17ac* knockout mice [37].

STXM images of zoomed-in region from the healthy control mouse kidney sample (same mouse as in Fig. 1a) but with TTE:MMHA resin embedding) are presented in Fig. 2. It should be noted that the STXM images are shown in OD, meaning that areas in light color transmit less photons in contrast to TEM imaging, where low electron transmittance leads to dark-colored areas. Panels a)–f) in Fig. 2 show images averaged over different energy intervals across the C 1s edge showcasing the drastic contrast changes and how different parts of the cell can be highlighted by selecting the X-ray imaging energy. Below the C 1s edge (Fig. 2a)), the contrast of the image is poor as it mostly here reflects the density and thickness variations across the section. As the section is stained, some contrast may originate from the density variations due to the staining agents prone to be attached to different parts of the tissue, e.g. OsO_4 to membranes due to its reaction with unsaturated lipids [45]. In Fig. 2b) averaged around 285 eV, a typical energy range for unsaturated and aromatic C 1s → π * transition in molecules present in biological matter [46], shows strongest absorption in the red blood cell (marked with '2'). Also, granular structures in the upper part of the image, which

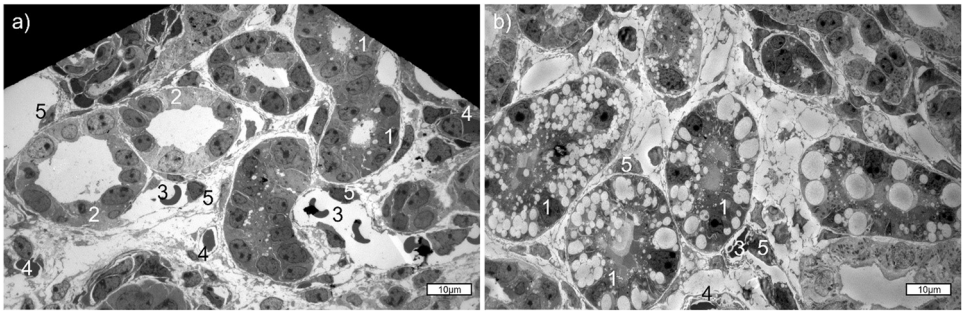

Fig. 1. TEM images of OsO_4 and uranyl acetate stained EPON embedded mouse kidney tissue. a) Healthy wild type mouse kidney. b) Disease mouse model kidney with numerous large and small vacuolar structures within the cells. Proximal tubules marked with 1, and distal tubules with 2. Red blood cells can be seen in venules 3 and capillaries 4. Nuclei of vascular endothelial cells are marked with 5.

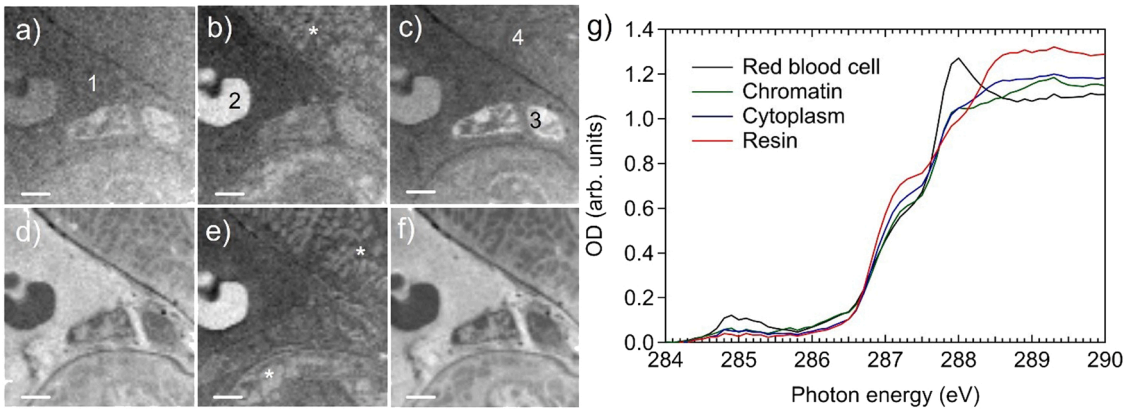

Fig. 2. OD images of OsO_4 and uranyl acetate stained TTE:MMHA embedded healthy control mouse kidney tissue. Each panel is the average OD for different energies at C 1s edge. The scale bars are 2 μm. a) 283.0–284.8 eV, b) 284.8–285.4 eV, c) 285.6–286.9 eV, d) 287.0–287.7 eV, e) 287.8–288.3 eV, f) 288.4–300.0 eV, g) Spectra from tissue components isolated from the scan area. Resin area marked with 1, red blood cell with 2, chromatin with 3 and cytoplasm with 4. Location of mitochondria is marked with * .

we interpret as mitochondria, become visible. In the next panel, Fig. 2c) showing the average of 285.6–286.9 eV, we interpret the most absorbing structure to be chromatin, a mixture of DNA and protein inside a cell nucleus (marked with '3'). The cell can be a vascular endothelial cell or a fibroblast or dendritic cell in the interstitial space between veins and tubules. In Fig. 2d), the embedding resin has the highest absorbance, and the red blood cell as well as thin membranes are nicely resolved. The contrast is completely flipped in the next energy interval 287.8–288.3 eV (Fig. 2e)), which contains the typical amide C1s $\rightarrow \pi^*$ transition energies and thus protein-rich red blood cell and mitochondria are highly absorbing. It is remarkable that now the chromatin structures are virtually not observed at all. The last STXM energy interval presented in Fig. 2f) is an average of energies above the absorption edge, and again the resin has the most absorbance. Chromatin is also visible, as well as membrane structures. X-ray absorption spectra of selected region of interests (ROIs) marked with numbers 1–4 to panels a)-c) are presented in Fig. 2g). TTE:MMHA resin spectrum extracted from the empty area has a broad absorption spectrum without clear sharp structures. It is to be noted that all the other spectra are now embedded on the top of the resin spectrum, but some distinct features can be still resolved. TTE:MMHA does not penetrate the whole tissue uniformly, making a subtraction of the background non-trivial task and resin subtraction was not carried out here. The spectrum taken from the red blood cell shows two clear peaks, at around 285 and 288 eV, typical energies for transitions in amino acids forming proteins. The spectra from cytoplasm and chromatin are more featureless, but even the subtle differences can lead to great contrast differences if proper energy intervals are examined, as shown in panels a)–f) of Fig. 2.

The spectra selected from the different parts the section shown in Fig. 2 can be used to produce SVD maps of the imaged region as shown in Fig. 3. An alternative option would be to use pure references of model compounds for SVD fits [47], but we opted here to use selected parts from the tissue itself. This has the benefit that it takes into account the chemical alteration due to sample preparation and diversity in macromolecular composition of certain region which is often overlooked when using model compounds. Fig. 3a), b), and c) show the fits of red blood cell, chromatin, and resin extracted spectra, respectively, and RGB map in Fig. 3d) the distribution of chemically similar parts of the section. As a result, protein-rich parts are shown in red (red blood cell and mitochondria), chromatin in green, and resin and cytosol in blue.

As mentioned earlier, staining is not a prerequisite for successful STXM imaging. Fig. 4 demonstrates a series of averaged images taken from a glomerulus of unstained wild type mouse kidney. Overview optical microscope image of the thin section is shown in Supplementary Material Fig. S1. Below the C 1s edge (Fig. 4a)) empty resin filled areas have the highest OD. In Fig. 4b) & d)), recorded at the same energy intervals where red blood cells showed the highest OD in Fig. 2b) & e), certain structures show up, which we thus interpret being red blood cells inside capillaries (also observed in Fig. 1. a). At these energies, cytoplasm and resin have similar OD whereas chromatin has the lowest. On energies ranging from 285.3 to 287.5 eV (Fig. 4c)) the image is similar to energies below the C 1s edge but with less noise, since in this energy interval there are no specific functional groups which would absorb strongly. There was no notable increase in OD for nucleus at 285.6–286.9 eV like there was in Fig. 2c). This can be due to difference of cell type or due to the effect of staining agents. Depending on the cell type, amounts of denser heterochromatin vs. less condensed euchromatin vary as the function of protein production activity of the cell [48].

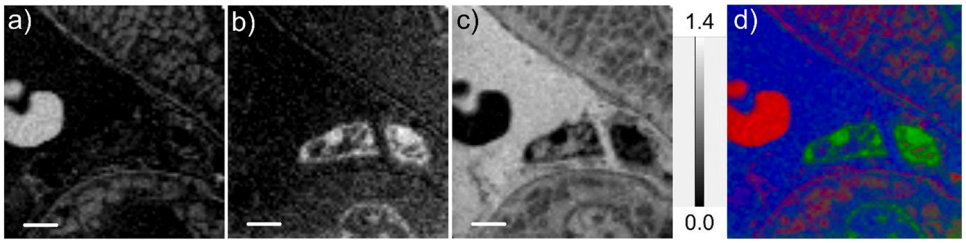

Fig. 3. SVD image of TTE:MMHA embedded healthy control mouse kidney tissue. SVD formed using the spectra of a) red blood cell, b) chromatin, c) resin, and d) is the color composite map of the three. The spectra are same as shown in Fig. 2. The scale bar is 2 μm.

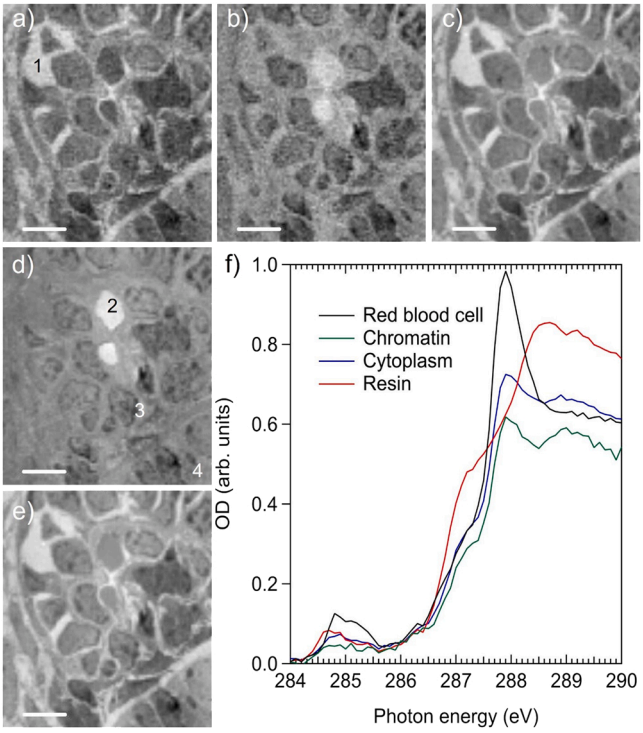

Fig. 4. OD images of TTE:MMHA embedded wild type mouse kidney tissue. Each panel is the average optical density for different energies on C 1s edge. The scale bars are 5 μm. a) 280.0–284.7 eV, b) 284.8–285.2 eV, c) 285.3–287.5 eV, d) 287.6–288.1 eV, e) 288.2–300.0 eV, f) Spectra from tissue components isolated from the scan area. Resin area marked with 1, red blood cell with 2, chromatin with 3 and cytoplasm with 4.

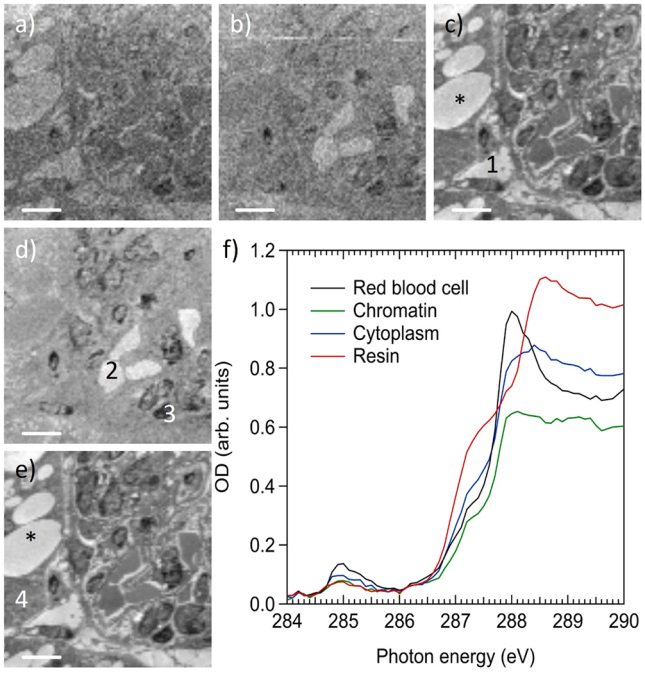

Fig. 5. OD images of TTE:MMHA embedded disease model mouse kidney tissue. Each panel is the average optical density for different energies on C 1s edge. The scale bars are 5 μm. a) 280.0–284.7 eV, b) 284.8–285.4 eV, c) 285.5–287.7 eV, d) 287.8–288.2 eV, e) 288.3–300.0 eV, f) Spectra from tissue components isolated from the scan area. Resin area marked with 1, red blood cell with 2, chromatin with 3 and cytoplasm with 4. Vacoules are marked with *.

At energies between 287.6 and 288.1 eV (Fig. 4d)) the difference between OD of red blood cells and chromatin compared to cytoplasm and resin is clearly visible. The same difference can be seen in the spectra presented in Fig. 4f). Above the absorption edge (Fig. 4e)) resin has the highest OD and the OD of red blood cells align with the OD of cytoplasm. The spectra in Fig. 2g) and 4f) are very similar for a similar ROIs no matter if the studied sample was stained or not. In unstained spectra, the peak at around 288 eV is more pronounced in red blood cell and also distinguished in chromatin and cytoplasm. This does not necessarily have anything to do with the staining but can be explained by a larger contribution of resin. This can also induce the small 0.1 eV shift between the highest peak position between spectra in Fig. 2g) and 4f). Thus, at least in these selected ROIs in different cells and cell organelles the staining does not seem to drastically alter the sample chemically.

To study how the defective *Slc17a5* affects the tissue morphology, kidney sections of the disease mouse model were imaged with STXM as shown in Fig. 5. Overview optical microscope image of the thin section can be found in Supplementary Material (Fig. S2.) In Fig. 5, large vacuoles are present on the left side of the images. The expectation was that the spectra extracted from vacuoles would have carried characteristics of sialic acid molecules corresponding to the accumulation material of SD. However, there was no noticeable difference between the spectra selected from ROIs in the vacuoles and outside the cells. The measured spectra corresponded to the resin spectrum suggesting that the material causing the formation of the vacuoles is no longer present. It is likely that the material is removed from the vacuoles during the sample preparation process. This can be due to SA being soluble to water. During the preparation process the samples are dried by gradually removing water with increasing concentration of ethanol and substituting it with the embedding material. This might be enough to remove most of SA even though sialin is normally required to transport SA over membranes [35]. Panels in Fig. 5a)–e) present the average ODs over different energy ranges across the C 1s edge. Red blood cells, resin, and chromatin can be differentiated at similar energies as in wild type mouse kidney presented in Fig. 4. The most remarkable phenomenon is again the almost exclusive contrast to red blood cells and chromatin in panels b) and d) of Fig. 5. This shows that even if the more water-soluble materials are removed by the sample preparation process, structural biomolecules remain and can be detected. There are some small

differences in energies where different parts can be detected the best between Figs. 4 and 5. It is possible that the embedding and curing process of TTE:MMHA is not completely uniform, leaving some variance in the resin spectrum. However, in this case it is most likely from using two different beamlines, as Figs. 4 and 5 were recorded at Soft*i*MAX and BL4U, respectively. Differences in reference resin spectrum can be seen when imaging at different beamlines even when using the same samples at both. The photon flux and respectively the dose at Soft*i*MAX is higher than at BL4U, which may have caused radiation damage related changes especially towards the higher energies of STXM recording. Also, proportion of higher order radiation getting through to the sample is a beamline specific property, which may make direct comparison of results less straightforward. Sample and its reference materials should be measured at same beamline to keep results consistent within an experiment. In data analysis, using reference data collected from multiple beamlines at different times can cause problems in data processing like subtracting the resin spectrum or doing SVD analysis of the components. Optimally the data processing should be done with reference data measured during the same experimental campaign as the samples were measured, as e.g. carbon contamination of optics evolve as a function of time. The major spectral features, e.g. peaks at ~285 eV and ~288 eV and post-edge continuum, have slightly varied relative intensities between experiments but their overall shape is similar, enabling spectroscopy based identification of cell organelles consistently between experiments. In Figs. 4 and 5, the energy regions have been adjusted to give the same visual contrast differences. Especially in the energy region of raising edge of the main absorption feature (287–289 eV), it is better to record a range of energies with a relatively small energy step, since the X-ray imaging contrast depends on small variations on relative X-ray absorption and a tiny offset in energy can lead to large contrast differences.

Fig. 6 presents SVD fits of red blood cell, chromatin, and resin and their color composite map of the same data as presented in Fig. 5. The ROIs where the spectra have been extracted are shown by 1–4 in Fig. 5. As described above, the spectrum from red blood cell marks protein-rich areas, also showing protein content in cytosol (red color in RGB map). Chromatin is marked with green, highlighting the nuclei while blue fitted with resin spectrum localize to vacuoles and interstitial space.

Spectromicroscopy at O 1s edge can also be used to image tissues. To demonstrate this with kidney tissue, OD images of the unstained healthy control mouse on O 1s edge are presented in Fig. 7. The overall absorbance is much lower at O 1s edge than C 1s edge as we used sections with the same thickness for both edges. Much lower amount of O in dry tissue compared to C would allow thicker sections for O 1s edge experiment. At lower 525.0–531.5 eV (Fig. 7a)) and higher 532.6–550.0 eV (Fig. 7c)) energy ranges the resin filled areas have the highest OD whereas at 531.6–532.5 eV (Fig. 7b)) red blood cell has the highest OD. The region around 532 eV corresponds to O1s → π * transition in amide [46]. There are not as many changes at different energies across the O 1s edge as with C 1s edge but the drastic contrast change that can be seen around 532 eV is similar to changes seen at 285 eV and 288 eV, and in line with the interpretation of these energies highlighting the protein-rich regions.

4. Liver

Liver is another organ taking part in the purification of blood stream, especially removing toxins. It also takes part in digestion by producing bile and produces e.g. hormones, glucose, and glycogen. Most of the cells in liver are hepatocytes, which are organized in plates separated by sinusoids. OD images of unstained disease model mouse liver tissue on C 1s edge are presented in Fig. 8. Overview optical microscope image of the thin section is shown in Supplementary Material Fig. S3. At lower energies below the absorption edge shown in Fig. 8a) the most prominent feature is the numerous vacuoles in the tissue which could be consistent with the *Slc17a5* edited mouse expressing a storage disease leading to accumulations in liver. However, the spectrum from the vacuoles shown in Fig. 8f) is similar to pure TTE:MMHA resin spectrum. Like in the case of disease mouse model kidney, this would indicate that whatever was in these vacuoles was substituted by the resin during embedding process. As the resin does not penetrate all the tissue the same way, the contrast below the C 1s edge highlights the resin regions with higher density than cells and cell organelles. In Fig. 8b) and d) around the peaks at 285 eV and 288 eV, respectively, the vacuoles disappear and the protein rich red blood cells in the capillaries become the prominent feature similarly to kidney in Fig. 5b) and d). At energies between these peaks shown in Fig. 8c) and above the absorption edge shown in Fig. 8e), the vacuoles are again the most prominent features, but the image is clearer than below the absorption edge in Fig. 8a). As seen in Fig. 8f), the resin like spectra in the vacuoles has dominant OD compared to other components except for around 285 and 288 eV correlating to aromatic and amide C 1s → π * transitions, respectively. This means that the resin is denser carbon material than rest of the cell structures. Also, chromatin OD is the lowest throughout the whole energy range showing as dark shape in the images. This shows that the resin is unable to penetrate chromatin as strongly as other cell materials leaving much lower OD than other cell structures. Chromatin has lower OD through the whole energy range as can be seen in Fig. 8f). This is similar to unstained kidney tissue in Fig. 4f) but differs from the stained kidney tissue in Fig. 2g).

Fig. 9 presents the OD images of TTE:MMHA resin embedded unstained control mouse liver tissue on O 1s edge. Overview optical microscope image of the thin section is shown in Supplementary Material Fig. S4. The overall contrast at O 1s edge is lower than at C 1s edge, but a few nuclei can still be resolved, one being right in the middle of the images. In general, the tissue looks more uniform compared to the disease model mouse in Fig. 8. A few vacuoles are still visible and are probably lipid droplets often found in liver. There are some narrow stripes in the bottom of the images due to section being a bit wrinkled on the film. Fig. 9a) shows an averaged image below the absorption edge, highlighting the denser resin areas inside vacuoles. Similarly to kidney O 1s results (Fig. 7), a clear difference can be seen around 532 eV energy range (Fig. 9b)), where red blood cells are highlighted (marked with '2'). The OD image of energies above 532.5 eV presented in Fig. 9c) is similar to below the edge image. The spectra presented in Fig. 9d) show how the contrast changes in OD originate from the π * resonance vs. main absorption edge ratio, red blood cells having highest absorption at around

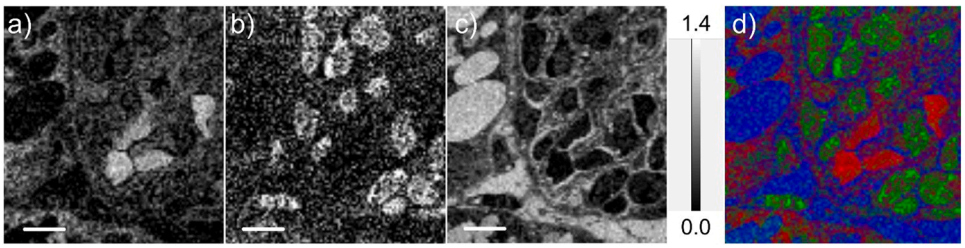

Fig. 6. SVD image of TTE:MMHA embedded disease mouse model kidney tissue. SVD formed using the spectra of a) red blood cell, b) chromatin, c) resin, and d) is the color composite map of the three. The spectra are same as shown in Fig. 5. The scale bar is 5 μm.

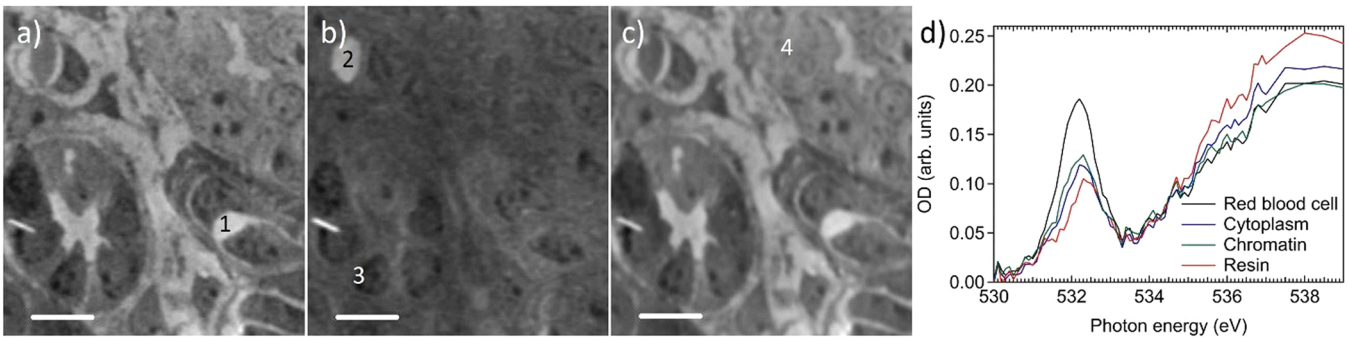

Fig. 7. OD images of TTE:MMHA embedded control mouse kidney tissue. Each panel is the average optical density for different energies on O 1s edge. The scale bars are 5 μm. a) 525.0–531.5 eV, b) 531.6–532.5 eV, c) 532.6–550.0 eV, d) Spectra from tissue components isolated from the scan area. Resin area marked with 1, red blood cell with 2, chromatin with 3 and cytoplasm with 4.

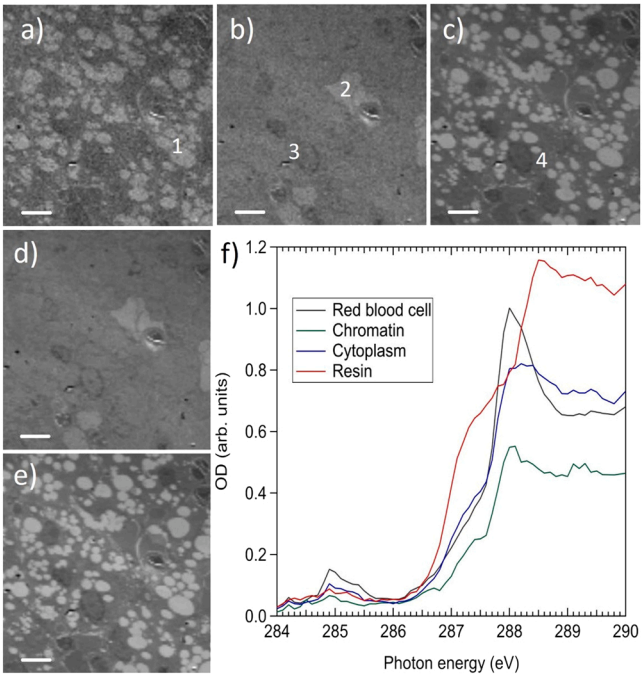

Fig. 8. OD images of TTE:MMHA embedded disease model mouse liver tissue. Each panel is the average optical density for different energies on C 1s edge. The scale bars are 5 μm. a) 282.0–284.7 eV b) 284.8–285.4 eV, c) 285.5–287.8 eV, d) 287.9–288.1 eV, e) 288.2–298.0 eV, f) Spectra from tissue components isolated from the scan area. Resin area marked with 1, red blood cell with 2, chromatin with 3 and cytoplasm with 4.

532 eV while being below cytosol and vacuoles at the rest of the energy range.

5. Conclusions

The potential of soft X-ray imaging of biological matter even in a wet state was recognized early on when the technique started to be developed, and recent advances are going towards 3D imaging with spectral or phase contrast. However, still today higher spatial resolution and resistance to radiation damage can be achieved with embedded thin sections compared to wet cells. Compared to TEM, the resolution is poorer, but on the other hand, thicker sections without staining can be used. We have presented soft X-ray spectromicroscopic imaging of mouse kidney and liver samples. We have shown that STXM reveals ultrastructural alterations in tissues due to storage diseases, with unexploited potential to chemical identification once sample preparation is streamlined to preserve material better. For cell culture samples, methods like wet cell measurements and fixing the cell on growth surface can be used to reduce the effects of sample preparations. However, tissue samples are too thick for STXM spectromicroscopic imaging with soft X-rays and require sectioning into thinner pieces while simultaneously keeping the cell structures intact. This requires some kind of structural support for the sectioning process which can be done with either embedding the samples in resin or by freezing them for cryosectioning. The embedding process might remove more soluble molecules from the sample as seen in this study, whereas cryo-sectioned samples are more susceptible for radiation damage compared to resin embedded samples as seen in our previous study.

We have identified energy regions where image contrast differences are the strongest due to rapidly changing absorption cross sections of different biomolecules. As a general observation, the optimal energies to get an overview of the tissue are either around 287 eV (absorption dip

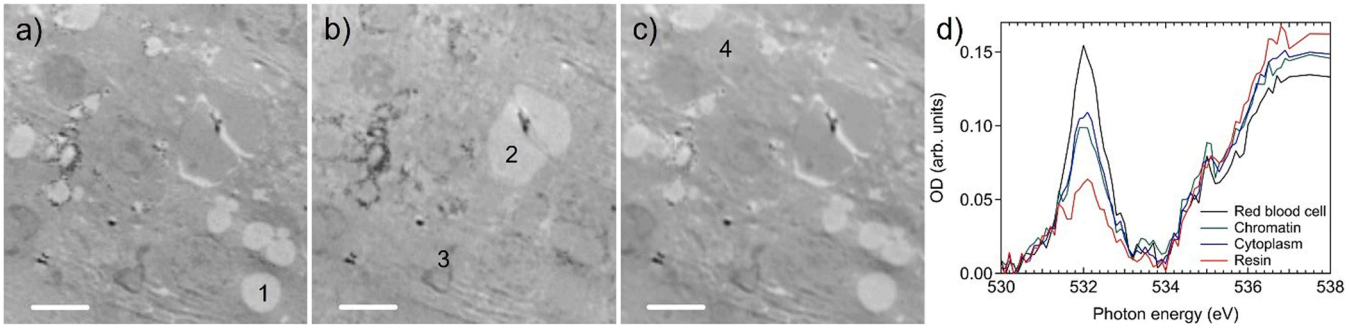

Fig. 9. OD images of TTE:MMHA embedded wild type mouse liver tissue. Each panel is the average optical density for different energies on O 1s edge. The scale bars are 5 μm. a) 525.0–531.5 eV, b) 531.6–532.5 eV, c) 532.6–550.0 eV, d) Spectra from tissue components isolated from the scan area. Resin area marked with 1, red blood cell with 2, chromatin with 3 and cytoplasm with 4.

between the aromatic and amide π * resonance regions) or above the absorption edge, whereas imaging around 288 eV emphasizes the protein rich regions and can provide a good contrast compared to embedding material. However, it should be noted that since the energy dependent contrast variations around 288 eV are large due to raising edges of typical embedding materials and macromolecules, the precise energies may vary. An extreme example of this can be seen in Fig. 2, where each energy interval seems to bring up a new feature of the kidney section. At O 1s edge, imaging at 532 eV is sensitive to protein-rich regions while best overall images are obtained above the absorption edge at 536 eV. The measurements can be concentrated to a few critical energies to avoid radiation damage and shorten the measurement time. Alternatively, the complete spectral information can be exploited using SVD analysis, which can emphasize and visualize structures which would otherwise be overwhelmed by e.g. embedding material. The imaging contrast is naturally the largest when accumulations have specific functional groups or bonds like C-S bonding targeted in a study of Parkinson's disease [27]. One of the drastic limitations related to medical research and diagnostics using soft X-ray spectromicroscopy or STXM is the availability of measurement time at synchrotron radiation facilities. However, there has been progress in several laboratories in development of tabletop soft X-ray sources and microscopes, which in future can provide easily accessible tools for soft X-ray spectromicroscopy. High-resolution, high intensity synchrotron radiation studies of different biological specimen serve as important benchmark for this development. An aspect which we have not exploited in this paper, but which is potentially very important in studies of storage diseases is the quantitative nature of STXM imaging. In future, when the sample preparation processing can reliably preserve the accumulating material, it could be also quantified based on the absorbance.

Declaration of Competing Interest

The authors declare that they have no known competing financial interests or personal relationships that could have appeared to influence the work reported in this paper.

Data Availability

Data will be made available on request.

Acknowledgements

A part of this work was performed at the BL4U of UVSOR Synchrotron Facility, Institute for Molecular Science (Proposals 22IMS6639, 19–836). We acknowledge Dr. Hayato Yuzawa for his help during the UVSOR III experiments.

We acknowledge MAX IV Laboratory for time on Beamline Soft*i*MAX under Proposal 20210845. We acknowledge Soft*i*MAX staff Karina Thånell, Igor Beinik, Jörg Schwenke and Claudiu Bulbucan for their assistance during the experiments. We also thank Md Thasfiquzzaman and Saku Paakkolanvaara for their help during the MAX IV experiments. Research conducted at MAX IV, a Swedish national user facility, is supported by the Swedish Research Council under contract 2018-07152, the Swedish Governmental Agency for Innovation Systems under contract 2018-04969, and Formas under contract 2019-02496.

We acknowledge EM-core, and Transgenic and Tissue Phenotyping Core Facility, Biocenter Oulu, a member of Biocenter Finland, for assistance in sample generation and preparation.

We acknowledge Biocenter Oulu (University of Oulu) "Emerging projects"-program and Jane and Aatos Erkko Foundation (FinnDisMice consortium: R.H., P.S., and S.K.) for funding.

This work was also partially supported by the Academy of Finland (Decision Numbers #331436 (J.U.), #296338 & #326291 (M.P.)), Pediatric Research Foundation, Finland (J.U. and R.H.), and Special State Grants for Health Research, Oulu University Hospital, Finland (J.U.).

The research was also partially supported by Magnus Ehrnrooth Foundation.

T.M. acknowledges funding from Tauno Tönning Foundation (20220043) and Emil Aaltonen Foundation (220134 N1).

Some authors of this publication are members of the European Reference Network on Rare Neurological Diseases (ERN-RND), Rare and Complex Epilepsies (EpiCARE), Neuromuscular Diseases (ERN-EURO-NMD) and Rare Congenital Malformations and Rare Intellectual Disability (ERN-ITHACA).

We acknowledge Prof. Adam Hitchcock for his help with aXis2000 software and valuable discussions and advice regarding STXM.

Appendix A. Supporting information

Supplementary data associated with this article can be found in the online version at doi:10.1016/j.elspec.2023.147368.

References

[1] W.C. Röntgen, On a new kind of rays, Nature 53 (1369) (1896) 274, https://doi.org/10.1038/053274a0.
[2] A.V. Baez, P. Kirkpatrick, Formation of optical images by X-Rays, J. Opt. Soc. Am. 38 (9) (1948) 766–774.
[3] P. Horowitz, J.A. Howell, A scanning x-ray microscope using synchrotron radiation, Sciences (80-.) 178 (4061) (1972) 608–611, https://doi.org/10.1126/science.178.4061.608.
[4] B. Niemann, D. Rudolph, G. Schmahl, X-ray microscopy with synchrotron radiation, Appl. Opt. 15 (8) (1976) 1883, https://doi.org/10.1364/ao.15.001883.
[5] G. Schmahl, D. Rudolph (Eds.), X-Ray Microscopy, Springer-Verlach, Berlin, 1984.
[6] H. Rarback, et al., Scanning x-ray microscope with 75-nm resolution, Rev. Sci. Instrum. 59 (1) (1988) 52–59, https://doi.org/10.1063/1.1139965.
[7] Y. Kagoshima, T. Miyahara, M. Ando, S. Aoki, Present status and future plan of soft x-ray microscopy at the Photon Factory, Rev. Sci. Instrum. 63 (1) (1992) 605–608, https://doi.org/10.1063/1.1142666.
[8] D. Morris, et al., Recent advances in scanning X-ray microscopy, Scanning 13 (1991) 7–10.
[9] H. Ade, X. Zhang, S. Cameron, C. Costello, J. Kirz, S. Williams, Chemical contrast in x-ray microscopy and spatially resolved XANES spectroscopy of organic specimens, Science (80-.) 258 (5084) (1992) 972–975, https://doi.org/10.1126/science.1439809.
[10] J. Kirz, C. Jacobsen, M. Howells, Soft X-ray microscopes and their biological applications, Q Rev. Biophys. 28 (1995) 33–130.
[11] X. Zhang, R. Balhorn, J. Mazrimas, J. Kirz, Mapping and measuring DNA to protein ratios in mammalian sperm head by XANES imaging, J. Struct. Biol. 116 (1996) 335–344.
[12] K. Shinohara, S. Toné, T. Ejima, T. Ohigashi, A. Ito, Quantitative distribution of DNA, RNA, histone and proteins other than histone in mammalian cells, nuclei and a chromosome at high resolution observed by scanning transmission soft X-ray microscopy (STXM), Cells 8 (2) (2019) 1–20, https://doi.org/10.3390/cells8020164.
[13] K. Shinohara, T. Ohigashi, S. Toné, M. Kado, A. Ito, Quantitative analysis of mammalian chromosome by scanning transmission soft X-ray microscopy, Ultramicroscopy 194 (2018) 1–6, https://doi.org/10.1016/j.ultramic.2018.07.001.
[14] J.R. Lawrence, et al., Scanning transmission X-ray, laser scanning, and transmission electron microscopy mapping of the exopolymeric matrix of microbial biofilms, Appl. Environ. Microbiol. 69 (9) (2003) 5543–5554, https://doi.org/10.1128/AEM.69.9.5543-5554.2003.
[15] J. Sedlmair, et al., Imaging of vascular smooth muscle cells with soft X-ray spectromicroscopy, Microsc. Microanal. 17 (6) (2011) 991–1001, https://doi.org/10.1017/S1431927611012165.
[16] R.C. Hunter, A.P. Hitchcock, J.J. Dynes, M. Obst, T.J. Beveridge, Mapping the speciation of iron in Pseudomonas aeruginosa biofilms using scanning transmission X-ray microscopy, Environ. Sci. Technol. 42 (23) (2008) 8766–8772, https://doi.org/10.1021/es801642z.
[17] T. Mansikkala, et al., Lignans in knotwood of Norway spruce: Localisation with soft x-ray microscopy and scanning transmission electron microscopy with energy dispersive x-ray spectroscopy, Molecules 25 (13) (2020) 2997, https://doi.org/10.3390/molecules25132997.
[18] C.A. Larabell, K.A. Nugent, Imaging cellular architecture with X-rays, Curr. Opin. Struct. Biol. 20 (5) (2010) 623–631, https://doi.org/10.1016/j.sbi.2010.08.008.
[19] A. Cossa, et al., Cryo soft X-ray tomography to explore Escherichia coli nucleoid remodeling by Hfq master regulator, J. Struct. Biol. 214 (4) (2022), 107912, https://doi.org/10.1016/j.jsb.2022.107912.
[20] G. Schmid, M. Obst, J. Wu, A.P. Hitchcock, X-ray and neutron techniques for nanomaterials characterization, in: C.S.S.R. Kumar (Ed.), X-ray and Neutron Techniques for Nanomaterials Characterization, Springer-Verlag, Berlin Heidelberg, 2016, pp. 43–93, https://doi.org/10.1007/978-3-662-48606-1.

[21] A.F.G. Leontowich, et al., Cryo scanning transmission x-ray microscope optimized for spectrotomography, Rev. Sci. Instrum. 89 (9) (2018), 093704, https://doi.org/10.1063/1.5041009.
[22] D.E. Bedolla, et al., Effects of soft X-ray radiation damage on paraffin-embedded rat tissues supported on ultralene: a chemical perspective, J. Synchrotron Radiat. 25 (3) (2018) 848–856, https://doi.org/10.1107/S1600577518003235.
[23] K. Yamamoto, et al., Selective probing of the penetration of dexamethasone into human skin by soft X-ray spectromicroscopy, Anal. Chem. 87 (12) (2015) 6173–6179, https://doi.org/10.1021/acs.analchem.5b00800.
[24] K. Yamamoto, et al., Core-multishell nanocarriers: transport and release of dexamethasone probed by soft X-ray spectromicroscopy, J. Control. Release 242 (2016) 64–70, https://doi.org/10.1016/j.jconrel.2016.08.028.
[25] K. Yamamoto, et al., Influence of the skin barrier on the penetration of topically-applied dexamethasone probed by soft X-ray spectromicroscopy, Eur. J. Pharm. Biopharm. 118 (2017) 30–37, https://doi.org/10.1016/j.ejpb.2016.12.005.
[26] G. Germer, et al., Improved skin permeability after topical treatment with serine protease: probing the penetration of rapamycin by scanning transmission X-ray microscopy, ACS Omega 6 (18) (2021) 12213–12222, https://doi.org/10.1021/acsomega.1c01058.
[27] J. Brooks, et al., Label-free nanoimaging of neuromelanin in the brain by soft X-ray spectromicroscopy, Angew. Chemie - Int. Ed 59 (29) (2020) 11984–11991, https://doi.org/10.1002/anie.202000239.
[28] J. Brooks, et al., Analysis of neuronal iron deposits in Parkinson's disease brain tissue by synchrotron x-ray spectromicroscopy, J. Trace Elem. Med. Biol. 62 (2020) 1–6, https://doi.org/10.1016/j.jtemb.2020.126555.
[29] N.D. Telling, et al., Iron Biochemistry is correlated with amyloid plaque morphology in an established mouse model of alzheimer's disease, Cell Chem. Biol. 24 (10) (2017) 1205–1215.e3, https://doi.org/10.1016/j.chembiol.2017.07.014.
[30] J. Everett, et al., Ferrous iron formation following the co-aggregation of ferric iron and the Alzheimer's disease peptide β-amyloid (1-42), J. R. Soc. Interface 11 (95) (2014) 20140165, https://doi.org/10.1098/rsif.2014.0165.
[31] J. Uusimaa, et al., The Finnish genetic heritage in 2022 – from diagnosis to translational research, DMM Dis. Model. Mech. 15 (10) (2022) dmm049490, https://doi.org/10.1242/dmm.049490.
[32] V. Papa, et al., The role of ultrastructural examination in storage diseases, Ultrastruct. Pathol. 34 (5) (2010) 243–251, https://doi.org/10.3109/01913121003780593.
[33] G. Parenti, D.L. Medina, A. Ballabio, The rapidly evolving view of lysosomal storage diseases, EMBO Mol. Med. 13 (2) (2021) 1–21, https://doi.org/10.15252/emmm.202012836.
[34] P. Aula, Salla disease, Arch. Neurol. 36 (2) (1979) 88, https://doi.org/10.1001/archneur.1979.00500380058006.
[35] N. Aula, et al., The spectrum of SLC17A5-gene mutations resulting in free sialic acid-storage diseases indicates some genotype-phenotype correlation, Am. J. Hum. Genet. 67 (4) (2000) 832–840, https://doi.org/10.1086/303077.
[36] R. Norio, The Finnish disease heritage III: the individual diseases, Hum. Genet. 112 (5–6) (2003) 470–526, https://doi.org/10.1007/s00439-002-0877-1.
[37] S. Stroobants, et al., Progressive leukoencephalopathy impairs neurobehavioral development in sialin-deficient mice, Exp. Neurol. 291 (2017) 106–119, https://doi.org/10.1016/J.EXPNEUROL.2017.02.009.
[38] T. Ohigashi, et al., Construction of the scanning transmission X-ray microscope beamline at UVSOR, J. Phys. Conf. Ser. 463 (1) (2013), 012006, https://doi.org/10.1088/1742-6596/463/1/012006.
[39] T. Ohigashi, N. Kosugi, Developments in sample environment for a scanning transmission X-ray microscope at UVSOR-III synchrotron, J. Electron Spectros. Relat. Phenom. 266 (2023), 147356, https://doi.org/10.1016/j.elspec.2023.147356.
[40] J. Schwenke, K. Thanell, I. Beinik, L. Roslund, T. Tyliszczak, SoftiMAX - a new Soft X-ray microscopy and coherent imaging beamline at the MAX IV facility, Microsc. Microanal. 24 (S2) (2018) 234–235, https://doi.org/10.1017/s143192761801351x.
[41] Y. Ma, C.T. Chen, G. Meigs, K. Randall, F. Sette, High-resolution K-shell photoabsorption measurements of simple molecules, Phys. Rev. A 44 (3) (1991) 1848–1858, https://doi.org/10.1103/PhysRevA.44.1848.
[42] G.R. Wight, C.E. Brion, K-shell energy loss spectra of 2.5 keV electrons in CO_2 and N2O, J. Electron Spectros. Relat. Phenom. 3 (5) (1974) 191–205, https://doi.org/10.1016/0368-2048(74)80010-1.
[43] A.P. Hitchcock, Analysis of X-ray images and spectra (aXis2000): A toolkit for the analysis of X-ray spectromicroscopy data, J. Electron Spectros. Relat. Phenom. 266 (2023), 147360.
[44] C. Jacobsen, S. Wirick, G. Flynn, C. Zimba, Soft X-ray spectroscopy from image sequences with sub-100 nm spatial resolution, J. Microsc. 197 (2) (2000) 173–184, https://doi.org/10.1046/j.1365-2818.2000.00640.x.
[45] J.J. Bozzola, L.D. Russel. Electron Microscopy: Principles and Techniques for Biologists, 2nd ed., Jones and Bartlett Publishers, Inc., Sudbury, 1999.
[46] J. Stewart-Ornstein, et al., Using intrinsic X-ray absorption spectral differences to identify and map peptides and proteins, J. Phys. Chem. B 111 (26) (2007) 7691–7699, https://doi.org/10.1021/jp0720993.
[47] K. Shinohara, A. Ito, T. Ohigashi, M. Kado, S. Toné, Discrimination of DNA and RNA distribution in a mammalian cell by scanning transmission soft X-ray microscopy, J. Xray Sci. Technol. 26 (6) (2018) 877–884, https://doi.org/10.3233/XST-180392.
[48] K.L. Huisinga, B. Brower-Toland, S.C.R. Elgin, The contradictory definitions of heterochromatin: Transcription and silencing, Chromosoma 115 (2) (2006) 110–122, https://doi.org/10.1007/s00412-006-0052-x.